1905–2005, J. W. Hedenquist, J. F. H. Thompson, R. J. Goldfarb, J. P. Richards, Eds. (Society of Economic Geologists, Littleton, CO, 2005), pp. 111–141.
17. L. G. Benning, T. M. Seward, *Geochim. Cosmochim. Acta* **60**, 1849 (1996).
18. A. Stefánnson, T. M. Seward, *Geochim. Cosmochim. Acta* **68**, 4121 (2004).
19. H. M. Bibby, T. G. Caldwell, F. J. Davey, T. H. Webb, *J. Volcanol. Geotherm. Res.* **68**, 29 (1995).
20. J. W. Hedenquist, S. F. Simmons, W. F. Giggenbach, C. S. Eldridge, *Geology* **21**, 731 (1993).
21. R. J. Andres, P. R. Kyle, R. L. Chuan, *Geol. Rundsch.* **82**, 687 (1993).
22. A. A. Longo, thesis, Oregon State University (2005).
23. B. I. A. McInnes, M. Gregoire, R. A. Binns, P. M. Herzig, M. D. Hannington, *Earth Planet. Sci. Lett.* **188**, 169 (2001).
24. D. Müller *et al.*, *Min. Dep.* **37**, 61 (2002).

25. We thank Lihir Gold Ltd. for field support, gold assays of deep drill cuttings, geothermal brine data, and permission to publish this manuscript. Research funding was provided by the Foundation for Research Science and Technology. Comments from P. R. L. Browne, J. W. Hedenquist, W. E. Seyfried, and N. C. White improved this manuscript.

21 July 2006; accepted 24 August 2006
10.1126/science.1132866

Cellular and Subcellular Structure of Neoproterozoic Animal Embryos

James W. Hagadorn,[1]* Shuhai Xiao,[2] Philip C. J. Donoghue,[3] Stefan Bengtson,[4] Neil J. Gostling,[3] Maria Pawlowska,[3] Elizabeth C. Raff,[5,6] Rudolf A. Raff,[5,6] F. Rudolf Turner,[5] Yin Chongyu,[7] Chuanming Zhou,[8] Xunlai Yuan,[8] Matthew B. McFeely,[1] Marco Stampanoni,[9] Kenneth H. Nealson[10]

Stereoblastic embryos from the Doushantuo Formation of China exhibit occasional asynchronous cell division, with diminishing blastomere volume as cleavage proceeded. Asynchronous cell division is common in modern embryos, implying that sophisticated mechanisms for differential cell division timing and embryonic cell lineage differentiation evolved before 551 million years ago. Subcellular structures akin to organelles, coated yolk granules, or lipid vesicles occur in these embryos. Paired reniform structures within embryo cells may represent fossil evidence of cells about to undergo division. Embryos exhibit no evidence of epithelial organization, even in embryos composed of ~1000 cells. Many of these features are compatible with metazoans, but the absence of epithelialization is consistent only with a stem-metazoan affinity for Doushantuo embryos.

Fossilized embryos in the 635- to 551-million-year-old Doushantuo Formation of South China provide a record of embryology during the emergence of animal phyla (*1*, *2*). Based on interpreted cellular layers and polar lobe–like structures (*3*–*7*), a suite of putative blastulae, gastrulae, larvae, and minute adults has been described from the deposit. These fossils may also house cellular- and organelle-scale details of cleavage patterns of early animals (*8*).

Unfortunately, taphonomic and diagenetic artifacts are abundant in Doushantuo embryos. These include postmortem evidence for differential cell shrinkage, cytoplasmic decay, loss of cells and embryo envelopes, patchy organic matter degradation, multiple episodes of botryoidal void-filling cementation and dissolution, clotted fabric development, geopetal infilling, ambient pyrite trail formation, and mineral overgrowth (*9*–*12*). These features are rarely visible on the surface of embryos and are difficult to resolve in individual thin sections or in embryos lacking complete embryo envelopes. To constrain interpretations of metazoan affinity and resolve internal structures in these embryos, we identified a suite of 162 relatively pristine envelope-bound and spheroidal embryos in which recurrent biological structures and cleavage patterns could be distinguished from inorganic artifacts. We then used x-ray computed tomography (CT) in concert with scanning electron microscopy (SEM), transmission electron microscopy (TEM), and thin-section petrography to examine their internal morphology in three dimensions. Because variations in x-ray attenuation within embryos typically correspond to mineralogical or density variations associated with cell boundaries, subcellular structures, and diagenetic cements (*13*–*15*), it was possible to screen samples and identify recurrent biological features. The cellular and subcellular architecture of each embryo was volume-rendered to determine the number, arrangement, shape, and volume of cells in each embryo, and then compared with SEM, TEM, and thin-section petrography of similar samples [see supporting online material (SOM)].

Several interpretations of Doushantuo embryos have assumed that they follow the canonical pattern of progressive and synchronous cleavage (*1*, *16*, *17*). Using image stacks of x-ray attenuation through each embryo, we extracted three-dimensional (3D) isosurface models of each cell and counted the number of cells, including unexposed cells (Fig. 1). Embryos composed of more than 64 cells were difficult to count owing to diagenetic homogenization of some cell boundaries; these and embryos exhibiting shrinkage or breakage were excluded from our analysis. Although many specimens follow the expected 2^n pattern ($n = 42$ out of 57 specimens), as many as one in four deviate from this pattern ($n \geq 9$), being composed instead of 3, 5, 7, 9, 15, 24, and 31 cells (Fig. 2, fig. S1, and movie S1). Aberrant numbers of cells have been noted in previous studies of Doushantuo embryos, and the "extra cell" has been interpreted as a polar lobe (*6*, *7*). However, this explanation becomes less likely in later-stage embryos, in embryos that have fewer than the expected number of cells, and in embryos that deviate more substantially from the canonical pattern.

Deviation from the canonical 2^n pattern can result from taphonomical, pathological, or developmental processes. Taphonomic loss of cells and pathologic production of unequal-sized cells can result from degradation, anoxia, and toxicity, but such patterns are irregular and probably variable among individuals of the same species (*18*). Thus, pathologic and taphonomic causes may be excluded at least for Doushantuo embryos with regularly shaped cells, leaving developmental control as a possible explanation. Perhaps metazoan cleavage was less well organized and constrained in the Neoproterozoic, in comparison to living metazoans. Noncanonical cell numbers in marine embryos can result from several developmental processes (see SOM). Many are peculiar to unequally cleaving embryos, resulting from differences in cell division machinery that produce a large and a small daughter cell rather than two equal-sized ones. In addition, noncanonical cell numbers can result from asynchronous timing as a normal part of equally cleaving cell lineages. Asynchronous cleavage of cell lineages is widespread among metazoans. In such marine embryos, a 2^n cleavage pattern is followed, but because not all cell lineages divide at the same rate, the numbers of cells at any time do not necessarily match this count sequence.

We examined serial x-ray attenuation slices through the *x*, *y*, and *z* axes of a number of 2- to 32-cell embryos in order to identify cells that have distinct subcellular structures (*6*, *8*, *12*, *14*). The structures are typically characterized by a

[1]Department of Geology, Amherst College, Amherst, MA 01002, USA. [2]Department of Geosciences, Virginia Polytechnic Institute and State University, Blacksburg, VA 24061, USA. [3]Department of Earth Sciences, University of Bristol, Bristol BS8 1RJ, UK. [4]Department of Palaeozoology, Swedish Museum of Natural History, SE-104 05 Stockholm, Sweden. [5]Department of Biology, Indiana University, Bloomington, IN 47401, USA. [6]School of Biological Sciences, University of Sydney, Sydney 2006, Australia. [7]Institute of Geology, Chinese Academy of Geological Sciences, Beijing, China. [8]State Key Laboratory of Paleobiology and Stratigraphy, Nanjing Institute of Geology and Paleontology, Chinese Academy of Sciences, Nanjing 210008, China. [9]Swiss Light Source, Paul Scherrer Institut, CH-5232 Villigen, Switzerland. [10]Department of Earth Sciences, University of Southern California, Los Angeles, CA 90089, USA.

*To whom correspondence should be addressed. E-mail: jwhagadorn@amherst.edu

different degree of x-ray attenuation than the surrounding cellular material, suggesting that they differ in composition or density from the matrix (Fig. 3). There are two types of intracellular structures. The first are small spheres seen in various kinds of embryos, including two- and three-cell embryos that preserve distinct membranes (Fig. 3A and movie S2). The spheres differ from clotted and botryoidal fabrics and are coated by layers with relatively high x-ray absorption. Some spheres exhibit evidence of collapse and deflation (Fig. 3C). Internally, they are either empty or have a lower degree of x-ray attenuation than the surrounding matrix, and thin-sectioned samples indicate that their interiors are more organic-rich than the matrix. Together these features are consistent with apatitic encrustation of degrading organic spheres, which are comparable in shape and size to membrane-bound cytoplasmic vesicles, lipids, or yolk granules in the cleaving blastomeres of metazoans such as demosponges (*19*) and echinoids (Fig. 3B).

The second group (n = 10) consists of spheroidal-to-reniform structures, present as one or two per cell, as revealed by isosurface modeling (Fig. 3, D to G, and movies S3 and S4). In contrast to the first type, these show a slightly higher x-ray attenuation than the surrounding matrix. Mirror-image pairs of these structures have been observed in all cells of a four-cell embryo (Fig. 3E), but in only one cell of another (fig. S2), and single intracellular structures exist in some cells of 3-, 4-, 8- and 16-cell embryos (Figs. 1 and 2C, figs. S1 and S3, and movie S5). Thin-section petrography and TEM of epoxy-embedded four-cell specimens bearing these structures were performed (Fig. 3, F and G) and reveal that the reniform structures are more electron-dense, which is consistent with relative x-ray attenuation values. Together, these observations suggest early diagenetic replacement of a compositionally distinct zone in the center of the cell, rather than later-stage cavity infilling.

There are two possible interpretations for these paired structures. First, they may represent inorganically precipitated diagenetic or taphonomic features. Intracellular structures are well known in coccoidal cyanobacterial cells preserved in cherts of the Bitter Springs Formation of Australia, and these have been interpreted as degraded cytoplasmic bodies because of their highly variable size and morphology (*20*–*22*). Indeed, some of the much smaller Doushantuo algal cells also contain intracellular structures with variable morphologies (Fig. 3H), and some Doushantuo embryo cells contain eccentrically located internal bodies covered with botryoidal encrustation [for example, see figure 3.7 of (*16*)] that are best interpreted as degraded cytoplasm. However, the reniform subcellular structures of Doushantuo embryos have consistent size, occurrence, and location among the studied population and have diffuse margins that grade into surrounding matrix. They may represent fossilized nuclei, spindle bundles, or other organelles (*8*, *14*). The size, shape, and mirrored orientation of paired intracellular structures in four-cell embryos are similar to those of spindle bundles or divided nuclei formed during karyokinesis in extant metazoan embryos (*23*). The long axis of the reniform bodies is parallel to an anticipated cell division plane, which might pass through the junction of the two largest polyhedral cell faces.

Rotation of each embryo's polyhedral cell models (movie S4) reveals the packing topology of cells. Two-cell embryos typically have hemispherical cells. In four-cell embryos, each cell typically has one convex face (the exposed exterior surface) and three planar faces that correspond to its three neighboring cells (Fig. 3E and fig. S2). Three-, five-, seven-, and nine-cell embryos reveal evidence of the rearrangement of cell topology between adjacent 2^n stages (Fig. 2E), bearing out inferences of flexibility in cell membranes (*17*). In eight-cell embryos, each cell has four or five neighbors and planar interfaces (fig. S3). In 16-cell embryos, one of

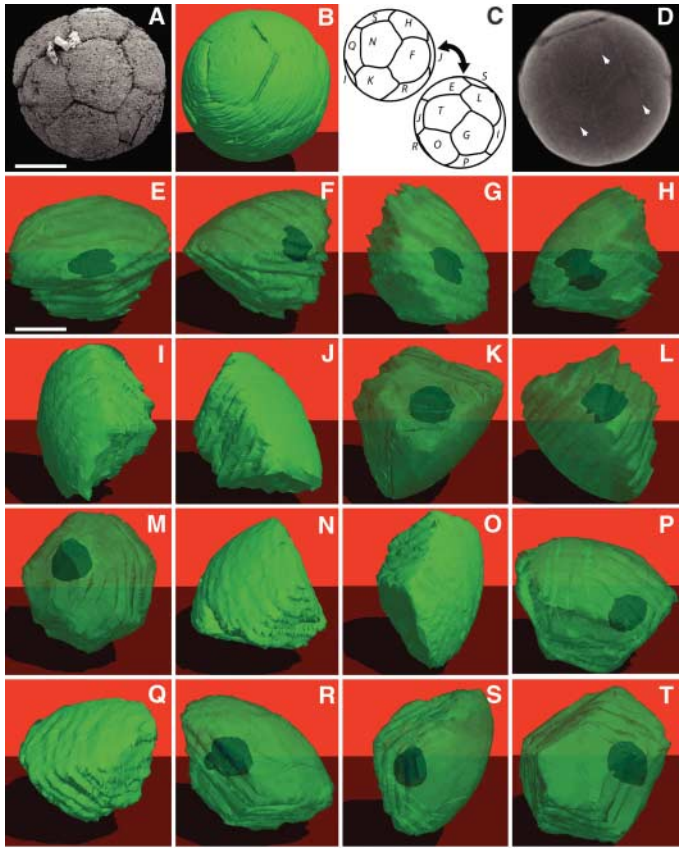

Fig. 1. (**A**) Scanning electron micrograph of a 16-cell embryo. (**B**) Isosurface model of the exterior of a 16-cell embryo (specimen DOU-10). (**C**) Schematic drawing with cells labeled to correspond to their models [(E) to (T)]. (**D**) An x-ray section showing very faint cell boundaries and subcellular spheroidal structures (arrowheads). Grayscale values in image have been inverted and the image placed on a black background to match (A). (**E** to **T**) Models of all 16 cells. Cells with intracellular structures (shaded dark green) are rendered transparent and those without are opaque. Corrugation on cell faces is an isocontouring artifact. (M) shows the internal cell. Scale bar in (A), 200 μm; in (E), 85 μm.

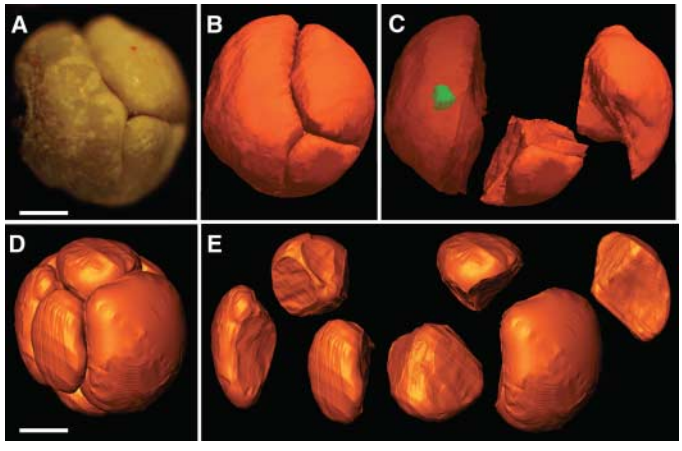

Fig. 2. Aberrant embryos. (**A**) Reflected-light photomicrograph of a 3-cell embryo (specimen DOU-25). (**B**) Exterior isosurface model. (**C**) Volume-rendered and extracted cell models, with the left cell rendered transparent to show the only subcellular structure (shaded green) in this embryo. (**D** and **E**) Seven-cell embryo (specimen MPLa). (D) Exterior isosurface model. (E) Volume renderings of each cell in (D). Cells in (C) and (E) are oriented in same position as they occur in (B) and (D). Scale bar in (A), 200 μm; in (D), 130 μm.

the cells sits in the center of the embryo and is surrounded by the remaining 15 cells, and thus has 15 planar faces (Fig. 1 and movie S5). The remaining exposed cells each have one convex exterior surface and six planar faces, which correspond to the five adjacent exposed cells and the internal cell. In embryos with ~32 cells, there are abundant many-faceted cells toward the exterior of the embryo, and many of these are more spheroidal than in earlier-stage embryos (movie S6). There are also several cells in the interior of each of these embryos, some of which are more elongate, pyramidal, or hourglass-shaped.

In many embryos composed of ~64 or more cells, the center is structureless, and embryos composed of hundreds to more than ~1000 cells still show no evidence of blastocoel formation or the organization of blastomeres into epithelia (fig. S4 and movie S7). Epithelialization, by whatever mechanism of gastrulation, should be underway in modern embryos with >100 cells.

The affinity of the embryos remains problematic because evidence of later developmental stages, juveniles, and adults is lacking, and because features in early developmental stages are often more widely distributed among animals than are those arising later in development (*24*). Despite hypotheses that Doushantuo embryos are unusual in comparison to most known metazoans (*25*), the patterns of cleavage and cell topology are compatible with a range of animal groups. For instance, in embryos composed of eight or more cells, the offset arrangement of successive tiers of cells, strong cell cohesion, and a stereoblastic cell topology are comparable to early cleavage embryos of many arthropod groups. Stereoblastulae are also particularly common among sponges (*26*) and scyphozoan cnidarians (*27*). Doushantuo embryos composed of many hundreds of cells resemble the purported gastrulae of demosponges, before the development of parenchymella larvae, although at this stage demosponges exhibit evidence of gastrulation, with a differentiated superficial layer of micromeres surrounding a core of macromeres (*19*).

None of the 162 embryos that we analyzed show any evidence of epithelial development. This absence of evidence is striking, given that the presence of subcellular structures in these fossils demonstrates a level of preservational fidelity comparable to that of the most celebrated fossil deposits (*28*). The absence of this 3D hallmark of sponge- and higher-grade metazoans (*29*, *30*) may indicate that they did not yet exist. Germ layers and tissue-grade structures suggested in Doushantuo microfossils (*3*–*5*) may instead be diagenetic artifacts (*9*–*11*). Together with topologic evidence and the absence of cell walls (*17*), which falsify an algal affinity, the combined observations suggest that the Doushantuo embryos are probably stem-group metazoans.

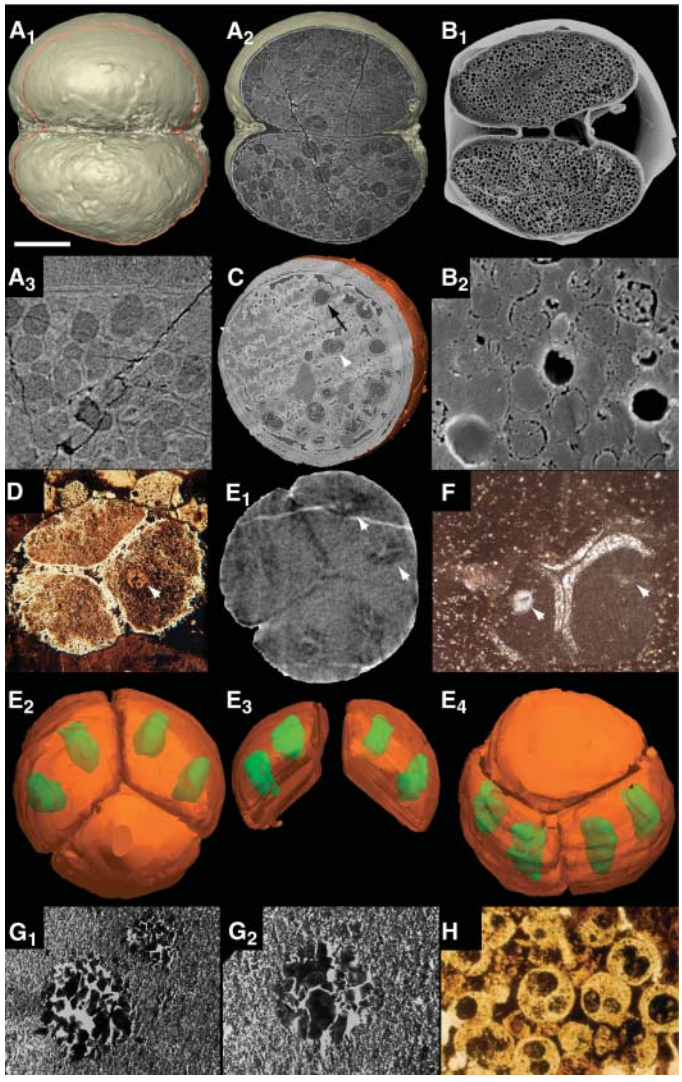

Fig. 3. (**A**) A two-cell embryo (specimen MPKxiv). (**A$_1$**) Surface rendering of the embryo based on tomographic scans, showing the position of the orthoslice (**A$_2$**), which reveals internal preservation of spheroidal subcellular structures analagous to modern lipid vesicles or yolk granules. (**A$_3$**) High magnification of an orthoslice at the boundary between the two cells. (**B$_1$** and **B$_2$**) Two-cell embryo of the sea urchin *Heliocidaris erythrogamma*, including an enlarged view of the lipid vesicles. Such vesicles are spheroidal and can be even larger in large-egged embryos of other modern invertebrates. (**C**) Orthosliced volume rendering of a possible embryo (specimen SB0604Clea), illustrating intact, deflated, and collapsed spheroidal and ovoidal interior structures, coated by several generations of cement. The left hemisphere is dominated by a clotted fabric. Representative deflated (white arrowhead) and collapsed (black arrow) spheres are indicated. Slices in (A) and (C) are negatives: Darker grayscale values represent lower x-ray attenuation. (**D** and **F**) Photomicrographs of four-cell embryos with subcellular structures (arrowheads). (F) Extracted, embedded, and thin-sectioned specimen. (**E$_1$**) X-ray section through a four-cell embryo (specimen DOU-8), showing three of the cells with paired subcellular structures (one pair is indicated by arrowheads), each with slightly greater attenuation (dark regions in image). (**E$_2$** to **E$_4$**) Isosurface models of the four tetrahedrally arranged cells, with two of the cells extracted. All cells have paired subcellular structures, but only the upper two cells are rendered transparent to show intracellular structures (shaded green). (E$_4$) Embryo from (E$_2$), rotated horizontally 180°. (**G**) TEM images of reniform (**G$_1$**) to spheroidal (**G$_2$**) structures like those in (D) to (F). Although the exact orientation of the embryo in (G$_1$) is poorly constrained because of difficulties inherent in sample embedding and microtoming, it is hypothesized that this represents a tangential section through a reniform subcellular structure, so that each kidney-shaped structure is represented by two subcircular, more electron-dense areas (dark regions in image). (**H**) Transmitted-light photomicrograph of much smaller algal or cyanobacterial cells, each with one or more intracellular structures that occupy much of each cell. Relative scale bar size is as follows: for (A) and (B), 170 μm; for (C), 270 μm; for (D), 150 μm; for (E), 150 μm; for (F), 190 μm; for (G$_1$), 8 μm; for (G$_2$), 5 μm; for (H), 20 μm.

References and Notes

1. S. Xiao, Y. Zhang, A. H. Knoll, *Nature* **391**, 553 (1998).
2. C.-W. Li, J.-Y. Chen, T.-E. Hua, *Science* **279**, 879 (1998).
3. J. Chen *et al.*, *Proc. Natl. Acad. Sci. U.S.A.* **97**, 4457 (2000).
4. J. Chen *et al.*, *Dev. Biol.* **248**, 182 (2002).
5. J.-Y. Chen, P. Oliveri, E. Davidson, D. J. Bottjer, *Science* **306**, 1291b (2004).
6. J.-Y. Chen, *The Dawn of Animal World* (Jiangsu Science and Technology Press, Nanjing, China, 2005).
7. J. Chen *et al.*, *Science* **312**, 1644 (2006).
8. P. Chien, J.-Y. Chen, C. W. Li, F. Leung, *PaleoBios* **21** (supplement to No. 2), 41 (2001).
9. S. Xiao, X. Yuan, A. H. Knoll, *Proc. Natl. Acad. Sci. U.S.A.* **97**, 13684 (2000).
10. S. Bengtson, G. Budd, *Science* **306**, 1291a (2004).
11. S. Bengtson, in *The New Panorama of Animal Evolution*, A. Legakis, S. Sfenthourakis, R. Polymeni, M. Thessalou-Legaki, Eds. (Pensoft, Moscow, 2003), pp. 289–300.
12. S. Q. Dornbos *et al.*, *Palaios* **21**, 3 (2006).
13. J. W. Hagadorn, K. H. Nealson, *PaleoBios* **21**, 60 (2001).
14. J. W. Hagadorn, S. Xiao, *Geol. Soc. Am. Ann. Meet. Abst.* **34**, 169 (2002).

15. P. C. J. Donoghue *et al.*, *Nature* **442**, 680 (2006).
16. S. Xiao, A. H. Knoll, *J. Paleontol.* **74**, 767 (2000).
17. S. Xiao, *Paleobiology* **28**, 244 (2002).
18. E. C. Raff, J. T. Vilinski, F. R. Turner, P. C. J. Donoghue, R. A. Raff, *Proc. Natl. Acad. Sci. U.S.A.* **103**, 5846 (2006).
19. S. P. Leys, B. M. Degnan, *Invertebr. Biol.* **121**, 171 (2002).
20. A. H. Knoll, E. S. Barghoorn, *Science* **190**, 52 (1975).
21. J. W. Schopf, *J. Paleontol.* **42**, 651 (1968).
22. J. K. Bartley, *Palaios* **11**, 571 (1996).
23. K. Kume, K. Dan, *Invertebrate Embryology* (Garland, New York, 1988).
24. K. E. von Baer, *Über Entwicklungsgeschichte der Thiere: Beobachtung und Reflexion* (Borntträger, Königsberg, Germany, 1828).
25. S. Conway Morris, *Curr. Opin. Genet. Dev.* **8**, 662 (1998).
26. P. E. Fell, in *Reproduction in Marine Invertebrates. Volume I: Aacoelomate and Pseudocoelomate Metazoans* (Academic Press, New York, 1974), pp. 51–132.
27. R. D. Campbell, in *Reproduction in Marine Invertebrates. Volume I: Acoelomate and Pseudocoelomate Metazoans* (Academic Press, New York, 1974), pp. 133–199.
28. D. M. Martill, *Nature* **346**, 171 (1990).
29. P. E. Fell, in *Embryology: Constructing the Organism*, S. F. Gilbert, A. M. Raunio, Eds. (Sinauer, Sunderland, MA, 1997), pp. 39–54.
30. E. A. Sperling, K. J. Peterson, *J. Geol. Soc. London,* in press.
31. We are grateful to the NSF, the National Geographic Society, National Natural Science Foundation of China, NASA, National Environment Research Council, National Endowment for Science Technology and the Arts, Leverhulme Trust, Mellon Foundation, Trustees of Amherst College, Swedish Research Council, and Chinese Academy of Geological Sciences for supporting this research, and to K. Claeson, C. Goutte, J. Kirschvink, M. Manning, K. Peterson, A. Tsapin, P. Williamson, and three anonymous reviewers for insightful comments and advice.

Supporting Online Material
www.sciencemag.org/cgi/content/full/314/5797/291/DC1
Materials and Methods
SOM Text
Figs. S1 to S4
Movies S1 to S7

27 July 2006; accepted 8 September 2006
10.1126/science.1133129

CDK2-Dependent Phosphorylation of FOXO1 as an Apoptotic Response to DNA Damage

Haojie Huang,[1,2]* Kevin M. Regan,[1,2] Zhenkun Lou,[3] Junjie Chen,[3] Donald J. Tindall[1,2]†

The function of cyclin-dependent kinase 2 (CDK2) is often abolished after DNA damage. The inhibition of CDK2 plays a central role in DNA damage–induced cell cycle arrest and DNA repair. However, whether CDK2 also influences the survival of cells under genotoxic stress is unknown. Forkhead box O (FOXO) transcription factors are emerging as key regulators of cell survival. CDK2 specifically phosphorylated FOXO1 at serine-249 (Ser^{249}) in vitro and in vivo. Phosphorylation of Ser^{249} resulted in cytoplasmic localization and inhibition of FOXO1. This phosphorylation was abrogated upon DNA damage through the cell cycle checkpoint pathway that is dependent on the protein kinases Chk1 and Chk2. Moreover, silencing of FOXO1 by small interfering RNA diminished DNA damage–induced death in both p53-deficient and p53-proficient cells. This effect was reversed by restored expression of FOXO1 in a manner depending on phosphorylation of Ser^{249}. Functional interaction between CDK2 and FOXO1 provides a mechanism that regulates apoptotic cell death after DNA strand breakage.

In response to DNA damage, mammalian cells activate checkpoint pathways that induce cell cycle delay or arrest. Delayed progression of the cell cycle allows time for either the repair of DNA damage or the elimination of genetically unstable cells by apoptosis. CDK2 is a key regulator of DNA damage–activated G_1 phase and intra–S phase checkpoints (*1*). DNA damage leads to the activation of several protein kinases, such as ataxia telangiectasia mutated (ATM), ataxia telangiectasia and Rad3 related (ATR), Chk1, and Chk2 (*2*), which eventually causes the p53-dependent transcription of the CDK inhibitor $p21^{WAF1}$ (*3*) or ubiquitin-dependent degradation of the protein phosphatase Cdc25A (*4*, *5*), or both, thereby inhibiting CDK2 activity and DNA replication. However, it is not clear whether CDK2 plays a role in the regulation of DNA damage–induced cell death.

[1]Department of Biochemistry and Molecular Biology, [2]Department of Urology, [3]Department of Oncology, Mayo Clinic College of Medicine, Rochester, MN 55905, USA.

*Present address: University of Minnesota Cancer Center, Minneapolis, MN 55455, USA.

†To whom correspondence should be addressed. E-mail: tindall.donald@mayo.edu

Activation of FOXO transcription factors induces apoptosis by up-regulating a number of cell death genes, including those encoding the ligand for the death receptor known as Fas or CD95, the Bcl-2–interacting mediator (*Bim*) of cell death, and the tumor necrosis factor–related apoptosis-inducing ligand (*6*–*8*). Increased expression of these pro-apoptotic proteins is required for cell death to be induced by the DNA damaging agent camptothecin or its derivatives (*9*, *10*). Because CDK2 is a key mediator of most checkpoint functions, we hypothesized that the activities of FOXO proteins might be regulated by DNA damage signals through functional interactions with CDK2. We therefore sought to determine whether CDK2 could phosphorylate the FOXO1 protein. Endogenous CDK2 proteins were immunoprecipitated from NIH 3T3 cells, and in vitro kinase assays were conducted with glutathione *S*-transferase (GST)–FOXO1 fusion proteins (Fig. 1A) as substrates. Two fragments of FOXO1, FO1-2 and FO1-3, were phosphorylated by immunoprecipitated CDK2 but not by control immunoprecipitates (Fig. 1B). The amount of FOXO1 phosphorylation was comparable to that of the C-terminal segment of retinoblastoma protein (RB), a well-characterized CDK2 substrate (Fig. 1B). No phosphorylation of the control GST protein was detected. Reconstituted complexes of purified bacterially produced GST-CDK2 with either GST–cyclin E or GST–cyclin A phosphorylated the same fragments of the FOXO1 protein as did the endogenous CDK2 (Fig. 1C). These effects were abolished when the CDK inhibitor $p27^{KIP1}$ was included (fig. S1A). These results indicate that CDK2 directly phosphorylates the FOXO1 protein in vitro.

CDK2 and other CDKs often recognize and phosphorylate the motif of serine or threonine followed by proline . Only one such site (Ser^{249}-Pro^{250}) exists in FO1-2. We demonstrated by in vitro kinase assays that CDK2 phosphorylates the FOXO1 protein at Ser^{249} and Ser^{298}, with a preference at Ser^{249} (Fig. 1D and fig. S1, C to E). These findings suggest that CDK2 phosphorylates FOXO1 primarily at the Ser^{249} residue within the consensus CDK-phosphorylation motif (fig. S1B).

To test whether FOXO1 is phosphorylated at Ser^{249} in vivo, we generated a phosphorylation-specific antibody against a peptide containing the phosphorylated Ser^{249}. The antibody specifically recognized the wild-type FOXO1 but not the Ser^{249}→Ala^{249} (S249A) mutant (Fig. 2A). This activity was blocked by a peptide containing the phosphorylated Ser^{249} but not by the corresponding nonphosphorylated peptide (fig. S2A). The antibody-mediated reaction was sensitive to the treatment of proteins with protein phosphatase (fig. S2B). Silencing of endogenous CDK2 by a pool of small interfering RNAs (siRNAs) led to a decrease in Ser^{249} phosphorylation (Fig. 2B). Moreover, phosphorylation of Ser^{249} was increased in cells transfected with an active CDK2 mutant, CDK2-Thr^{14}→Ala^{14}-Tyr^{15}→Phe^{15} (CDK2-AF), that is unable to undergo inhibitory phosphorylation (*5*) (fig. S2C). Furthermore, phosphorylation of Ser^{249} was low during the G_1 phase and increased as cells progressed through the S phase (Fig. 2C). Thus, these data indicate that CDK2 phosphorylates FOXO1 at Ser^{249} in vivo. CDK2 also interacts with the FOXO1 protein in vitro and in vivo (fig. S3).

FOXO1 functions primarily as a transcription factor. Ectopic expression of CDK2 and